

Alkaline CO electro-oxidation: Mechanistic Differences between Copper and Gold Single Crystals and Peculiarities of various Copper Facets

Aarti Tiwari,^{†,‡,||} Nitish Govindarajan,^{¶,||} Hendrik H. Heenen,[¶] Anton Bjørnlund,[†]
Karen Chan,^{*,¶} and Sebastian Horch^{*,†,§}

[†]*SurfCat, Department of Physics, Technical University of Denmark, 2800 Kgs. Lyngby, Denmark*

[‡]*Interface Science Department, Fritz-Haber Institute of the Max Planck Society, 14195 Berlin, Germany*

[¶]*Catalysis Theory Center, Department of Physics, Technical University of Denmark, 2800 Kgs. Lyngby, Denmark*

[§]*Department of Engineering Technology, Technical University of Denmark, 2750 Ballerup, Denmark*

|| These authors contributed equally to this work

E-mail: kchan@fysik.dtu.dk; shor@dtu.dk

Abstract

Understanding CO electro-oxidation is crucial towards designing catalysts for electrochemically oxidizing complex organic molecules. Earth-abundant Copper (Cu) has recently been demonstrated to exhibit high alkaline CO electro-oxidation activity, rivaling the previously acclaimed Gold (Au). Herein, we combine single crystal rotating

disc electrode (RDE) experiments and *ab initio* microkinetic modeling to understand the underlying reaction mechanisms on Cu and Au surfaces. Cu exhibits a facet-dependent activity with Cu(111) having a 0.27 V lower overpotential than Au(111) and a comparable CO oxidation current density. Using Koutecky-Levich analysis and DFT based microkinetic modeling, we identify the rate-limiting pathway to be Langmuir-Hinshelwood on Cu whereas Eley-Rideal on Au. We additionally present strikingly variant RDE responses on four Cu facets (111, 100, 110 and 211) and long-term stability analysis on Cu(111) and Au(111). We find a combined reset-reaction profile helps Cu retain its high activity and pose a strong competition to the expensive Au catalysts.

The oxidation of CO to CO₂ has been extensively studied on several catalysts both in the context of thermal and electro-catalysis.¹⁻³ The electrochemical process (e-COOR) has both fundamental and technological relevance. For instance, it has been used to understand pH dependence in electrochemical reactions,⁴ it occurs in the electro-oxidation of biomass derived molecules⁵ and can be applied to remove CO impurities from reactant streams to avoid poisoning of electrodes used in direct alcohol fuel cells.^{6,7} CO thus has an ambivalent role in electrocatalysis being a central intermediate in many reactions on the one hand and a disruptive contaminant on the other.

In this article, we focus on the e-COOR, where both the intricate adsorption dynamics of CO and its subsequent coupling with OH, leading to the oxidation of CO, have been identified as important aspects.^{8,9} These aspects have already been extensively investigated on Platinum (Pt)—one of the most active monometallic electrocatalysts for fuel cell applications.¹⁰ Pt is prone to poisoning by CO via the blocking of active sites upon its exposure either as a reaction intermediate or an adventitious entity, for example during electrocatalytic operation.⁸ The poisoning effect of CO on Pt has been the focus of research for decades,¹¹ and CO tolerant alternatives including bimetallic alloys of Pt¹² or other cost-effective elements have been reported.¹³ CO poisoning therefore necessitates electro-oxidation catalysts to also be capable of performing e-COOR in order to retain their activity. This approach has

been exemplified by combining Pt with Ru where the latter supplies adsorbed *OH species to react with *CO species on the former to facilitate e-COOR^{14,15} and also reactivates the poisoned Pt.^{16,17}

In the search for more CO-tolerant e-COOR catalysts, Au has hitherto been demonstrated as the most active catalyst in alkaline media, with an onset potential that is ca. 0.5 V lower than Pt. In addition, the e-COOR activity on Au is not short lived unlike Pt due to its weak interaction with CO, thereby avoiding surface poisoning.¹⁸ Ever since the first observation of Au as an active e-COOR catalyst by Kita et al.,¹⁹ several studies aiming to understand the origin of the high activity of Au towards CO electro-oxidation have been reported.^{2,18,20} It is only recently that our work²¹ together with Kunze et al.²² has demonstrated earth abundant Cu to rival the activity of Au for alkaline CO electro-oxidation, thereby opening new avenues for this important reaction. The reason for the low overpotentials of Cu towards e-COOR has been attributed to the following experimental and theoretical findings:

1. The ability of different Cu facets to have a significant *OH coverage²³ before the equilibrium potential for e-COOR (ca. -0.1 V vs. RHE)
2. Favorable CO adsorption energetics on Cu surfaces
3. The co-existence of *CO and *OH in the relevant potential range to allow for the formation of the *COOH intermediate with surmountable barriers leading to the final oxidation product (CO₂)

While these interesting findings have led to an initial understanding of the origin of the high e-COOR *activity* on Cu, a pertinent question remains to be answered: how do the *kinetics* of e-COOR on Cu compare to Au? To answer this, we present a combined theoretical-experimental study of e-COOR on well-defined Au and Cu single crystals (SCs). We first show the fundamental electrochemical response on Cu and Au SCs both in the absence and presence of CO, and then combine RDE experiments with density functional theory (DFT) based microkinetic modeling to evaluate the differences in their respective

e-COOR mechanism. While we mostly concentrate on the (111) facet when comparing e-COOR, we also present the RDE response on other fundamental Cu facets, namely (100), (110) and (211), which turn out to be strikingly different. Finally, we explore and optimize the parameters to achieve long term stability (20 h) for alkaline e-COOR, which has rarely been pursued even for the well studied Au electrodes.

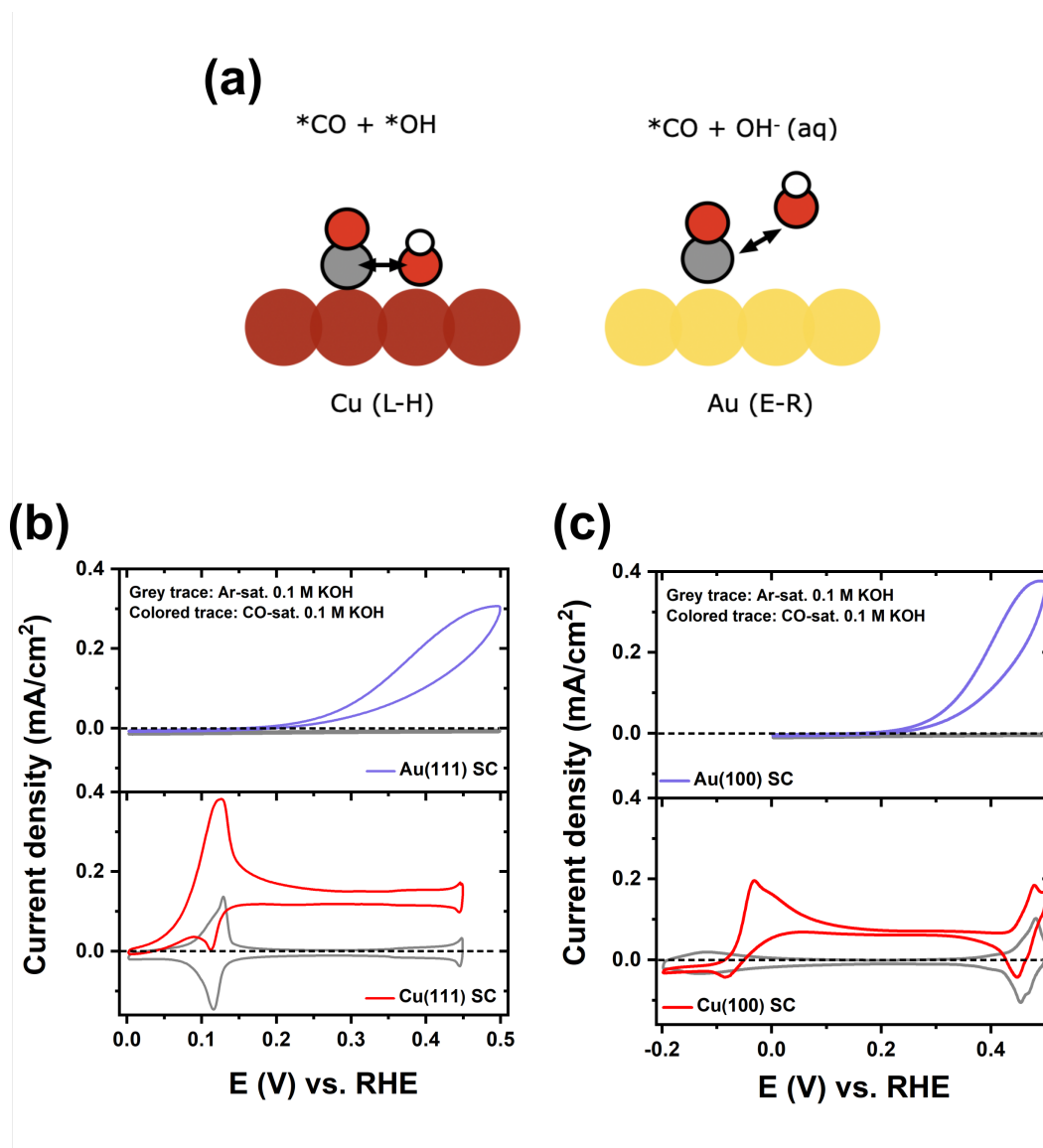
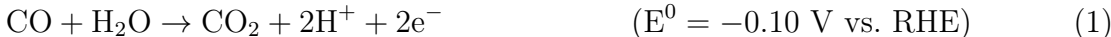


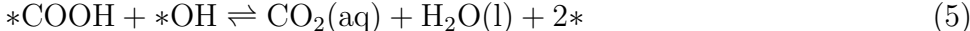
Figure 1: (a) Schematic for the proposed rate-determining step (RDS) for alkaline e-COOR on Cu and Au SCs involving the Langmuir-Hinshelwood (L-H) and Eley-Rideal (E-R) coupling pathways. Cyclic voltammograms for (b) Au & Cu(111), and (c) Au & Cu(100) SCs measured in blank Ar-saturated (grey trace) and CO-saturated (colored trace) 0.1 M KOH at a scan rate of 50 mV/s.

To set the stage, Figure 1a presents the proposed rate-determining step (RDS) for alkaline e-COOR on Cu and Au SCs as identified from our rotating disc electrode (RDE) experiments and DFT based microkinetic modeling (*vide infra*). As already suggested in previous studies on Cu SCs,^{21,22} our kinetic analysis confirms that the CO-OH coupling proceeds via a Langmuir-Hinshelwood (L-H) pathway (a chemical step), while it proceeds via an Eley-Rideal (E-R) pathway (an electrochemical step) on Au SCs, in agreement with previous studies on Au surfaces.^{18,20}

The overall e-COOR is given by:



Proposed e-COOR mechanism on Cu:



Proposed e-COOR mechanism on Au:



For e-COOR on Cu, the adsorption of the OH species (*OH) is the sole electrochemical step. In contrast, on Au, both the E-R rate-determining step involving an OH⁻ species and the formation of CO₂ are electrochemical.² We will now detail the experimental and computational kinetic studies that led us to the proposed rate-determining steps for alkaline

e-COOR on Cu and Au SCs.

Experimentally, we first measured cyclic voltammograms (CVs) on Cu and Au SCs to compare their respective e-COOR ability. [Figure 1b & c](#) show that for both Cu and Au SCs, the presence of CO(g) gives rise to a distinct oxidation current vs. the Ar-saturated case, which indicates the occurrence of e-COOR^{21,22} (cf. Section 1.1, SI for setup details²⁴ and measurement parameters). Similar CV traces for Cu (110) and (211) are shown in [Figure S1](#) (SI). We observe that CO electro-oxidation on both Cu(111) & Cu(100) start at a potential closer to the equilibrium potential (ca. -0.1 V vs. RHE) compared to the respective Au facets ([Figure 1b & c](#)), which suggest Cu to be a relatively better e-COOR catalyst than Au. The respective onset and overpotentials (η) for Cu and Au SCs are provided in [Table 1](#) and [Table S1](#) (SI). To further evaluate the impact of mass transport limitations and understand the reaction kinetics, we performed RDE measurements. [Figure 2a & b](#) show a direct comparison between the e-COOR polarization curves for the (100) and (111) facets of Cu and Au. At the outset, Au SCs reveal a typical sigmoidal behavior with negligible hysteresis. On the contrary, Cu facets have strikingly different polarization curves with a distinct hysteresis suggesting that the steady-state coverage of adsorbates vary on a reduced vs. partially oxidized surface.²⁵

Table 1: Experimentally observed onset (E_{onset}) and overpotential (η) corresponding to 1 mA/cm² along with the diffusion limited current density at 900 rpm (j) taken at 0.3 V for Cu SC and 0.6 V for Au SC from [Figure 2a & b](#).

<i>Surface</i>	$E_{\text{onset}}(V)$	$\eta(V)$	$j(\text{mA}/\text{cm}^2)$
Cu(111)	0.05	0.15	0.97
Au(111)	0.27	0.37	1.48
Cu(100)	-0.05	0.05	0.27
Au(100)	0.31	0.41	1.39

Notable quantitative e-COOR outcomes from [Figure 2a & b](#) are given in [Table 1](#) when compared at 900 rpm. Cu(111) exhibits superior e-COOR onset potential with an $\eta \approx 220$ mV lower than Au(111), while the current density (j) on Au(111) is ca. 1.5 times higher than Cu(111). On the other hand, the onset potential of Cu(100) is ca. 360 mV lower than

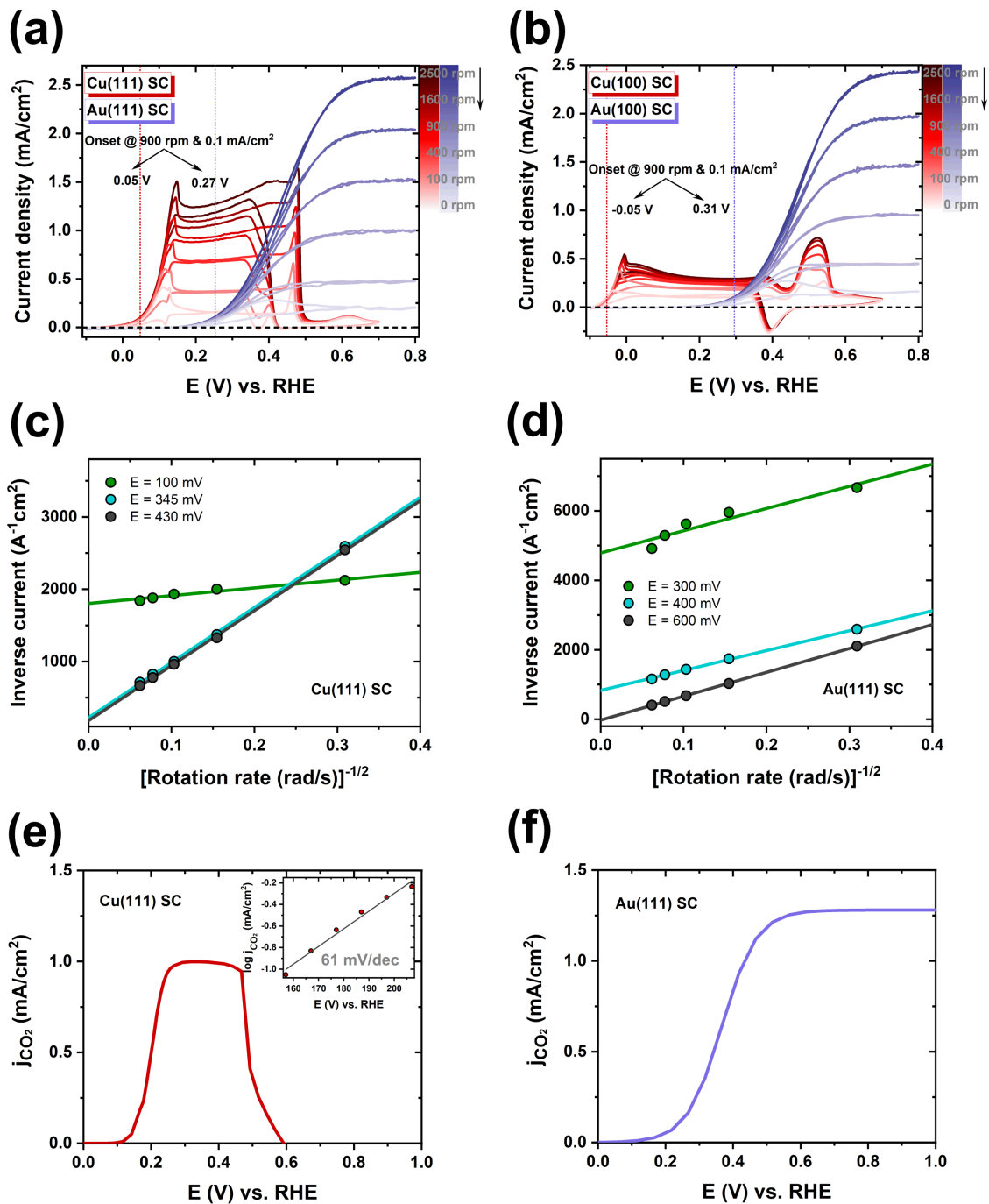


Figure 2: Polarization curves for Cu and Au SCs on the (a) (111) and, (b) (100) facets respectively in CO saturated 0.1 M KOH from 2500 to 100 rpm at a scan rate of 25 mV/s. Cu and Au are co-plotted here for easier comparison, in addition to a 0 rpm trace to visualize the effect of rotation. (c & d) Koutecky-Levich plot for Cu(111) and Au(111) SCs respectively. Simulated CO₂ polarization curves for e-COOR on (e) Cu(111) with the simulated Tafel slope (61 mV/dec) close to the onset potential shown in the inset and (f) Au(111), both obtained using DFT based microkinetic modeling simulations.

Au(100), albeit with a significantly lower j . Hence, both Cu SCs offer low overpotentials towards e-COOR and both Au SCs offer higher j . However, considering both the aspects of onset and j an optimal activity is observed over Cu(111).

The RDE results from [Figure 2a](#) were further analyzed to extract the kinetics and mechanistic information for alkaline e-COOR on the (111) facet of both Cu and Au. Firstly, Koutecky-Levich plots shown in [Figure 2c,d](#) were constructed using the Koutecky-Levich equation (cf. [Equation \(9\)](#)).

$$\frac{1}{j_L} = \frac{1}{j_K} + \frac{1}{j_D} \tag{9}$$

$$j_D \propto \omega^{-1/2} \tag{10}$$

Here, j_L is the limiting current density, j_K is the kinetic current density and j_D is the diffusion-limited current density that is related to the rotation rate (ω) (cf. [Equation \(10\)](#)). For Au(111), the Koutecky-Levich plot has a y-axis intercept ≈ 0 at 0.6 V, which suggests that only diffusion limitations govern the obtained current density at this potential. Conversely, Cu(111) has a non-zero intercept at ca. 0.4 V, indicating that even if the rotation rate is infinite, e-COOR will still have kinetic limitations for potentials ≥ 0.4 V. Further, j_k in the absence of any mass transport limitations used to construct the Tafel plots ([Figure 9](#), SI) are obtained from the Koutecky-Levich plot intercepts at different potentials. The estimated Tafel slope for Cu(111) is 70 mV/dec ([Figure 9a](#), SI) suggesting the rate-limiting coupling of *CO and *OH after the first electron-transfer step [Equation \(4\)](#) (i.e. there is a Nernstian shift in activity w.r.t potential vs. SHE, corresponding to the change in *OH coverage with potential). In contrast, Au(111) exhibits a Tafel slope of 125 mV/dec ([Figure 9b](#), SI), suggesting a rate-determining coupling of *CO and OH⁻ in the first electron-transfer step ([Equation \(7\)](#)) with a typical transfer coefficient between 0 and 1. The measured Tafel slope for Au(111) is in agreement with previous alkaline e-COOR studies.^{18,20}

Additionally, DFT based microkinetic modeling was performed to obtain the simulated polarization curves for e-COOR on Cu(111) and Au(111). The details of the computational setup and simulations are provided in Section 2 (SI). The (chemical) association barriers of *CO and *COOH with *OH on Cu(111) was determined explicitly using DFT simulations (Figure S7, SI). Given the challenges associated with estimating electrochemical barriers including solvent effects and DFT simulations at a constant potential,²⁶ we fit the barrier for the electrochemical coupling of *CO and OH⁻ on Au(111) to match j_k obtained using Levich analysis (cf. Figure 2d). For this fit, the charge transfer co-efficient, β for the CO-OH⁻ coupling was assumed to be 0.5 (following the experimental Tafel slope of 125 mV/dec, Figure 9b, SI). Mass transport of CO(aq) was accounted with a Fickian diffusion model through a boundary layer of thickness $\approx 10 \mu\text{m}$. We note that the boundary layer thickness has an effect on the magnitude of j_D but the overall simulated polarization curve features remained unchanged (cf. Figure S10, SI). Figure 2e & f, shows the simulated current density towards CO₂ (j_{CO_2}) on Cu(111) and Au(111) agreeing qualitatively with the RDE experiments (cf. Figure 2a & b). The simulated CO₂ polarization curves show e-COOR as entirely diffusion limited on Au(111) even at potentials $> 0.6 \text{ V}$, while Cu(111) is inactive. The latter arises from poisoning of Cu(111) due to the build-up of *OH species with increasing anodic potentials. Note that we do not consider surface oxidation reactions in our microkinetic model. Further, for Cu(111), we find the (chemical) coupling of *CO and *OH to be the rate-determining step close to the e-COOR onset potential as confirmed by a degree of rate control (DRC) analysis (Figure S11, SI).²⁷ This results in a simulated Tafel slope of 61 mV/dec (cf. Figure 2e, inset) which agrees with the measured Tafel slope of 70 mV/dec (Figure 9a, SI).

Having thus established the underlying differences between Cu and Au towards e-COOR, we now present the facet-specific RDE responses on Cu. Figure 3 shows a complex facet-dependent RDE behaviour whose features as exemplified by the Cu(111) surface (Figure 3a) are interpreted as: (i) The first peak (at ca. 0.14 V) corresponds to OH adsorption on

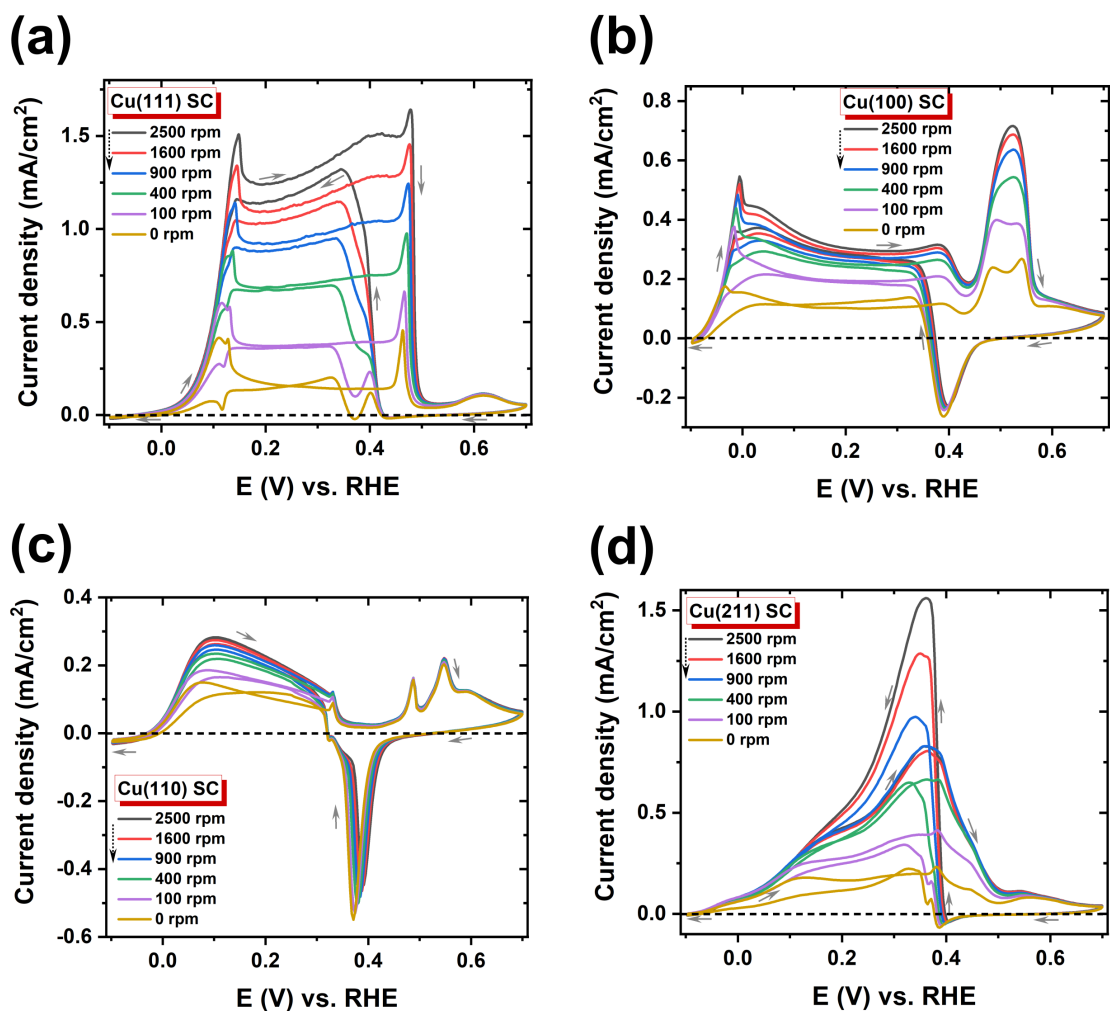


Figure 3: Polarization curves for (a) Cu(111), (b) Cu(100), (c) Cu(110), and (d) Cu(211) SCs in CO saturated 0.1 M KOH from 2500 to 0 rpm at a scan rate of 25 mV/s. Note the different y-axis.

Cu(111).^{21,28} (ii) The second peak (at ca. 0.47 V) corresponds to the beginning of surface oxidation.²⁹ (iii) The subsequent oxidative peak at ca. 0.6 V denotes progressive oxidation of Cu(0) to Cu(I) species³⁰ without any CO oxidation current [similar response to Ar-purged electrolyte; Figure S3a and S4a, SI]. (iv) On the reverse sweep, the surface first undergoes reduction (at ca. 0.4 V) and then regains its CO oxidation activity. (v) Compared to Au (cf. Figure 2a & b), a prominent hysteresis is observed between the forward and reverse trace on Cu(111). Similar characteristics, albeit with different features, are observed for

Cu(100), Cu(110) and Cu(211) [cf. Section 1.2, SI]. Notably, enhanced mass transport only marginally increased the e-COOR current densities for Cu(110) whereas, Cu(211) exhibits relatively higher current densities on the reverse sweep (at ca. 0.34 V) suggesting that a freshly reduced surface is more active for e-COOR. A detailed investigation of these facet dependent features for e-COOR on Cu SCs warrants a separate study of its own.

Finally, we address the long-term stability that, besides the electrocatalytic activity and reaction kinetics discussed above, is crucial to evaluate the overall performance of a catalyst. In the following, we focus on the stability of Cu(111) and Au(111) towards e-COOR. As seen from Figure 4a, even upon continuous cycling between -0.1 to +0.7 V, a significant CO oxidation activity on Cu(111) is retained for 20 h. However, Figure S5a (SI) clearly reflects progressive changes in the polarization curve with time, which could be attributed to variable coverage of the reactant, intermediates and product species on the catalyst surface,²¹ causing every potentiodynamic cycle to be affected by the history of the previous oxidative cycle. This aspect suggests if one could somehow reset the surface, it might be possible to retain the e-COOR activity. Considering these aspects and the fact that an oxidized Cu surface is inactive towards e-COOR but a freshly reduced surface is activated (Figure 3), another potential profile was designed. The first 10 cycles were measured between -0.1 to +0.7 V (reaction) followed by 2 cycles from -0.1 to +1.0 V (reset). A repetition of this specific combination of two potential profiles (reaction and reset) for 20 h lead to a long term retention of the CO oxidation activity for Cu(111) as shown in Figure 4b and Figure S5b (SI). In contrast, potentiodynamic cycling between -0.1 to +1.0 V for 20 h on Au(111) shows a relatively stable e-COOR response (Figure 4c and S5c, SI) without the need for a reset potential as compared to Cu(111). These differences can be attributed to the higher surface oxidation potential and weaker interaction of CO with Au(111) compared to Cu(111).

In summary, we investigated alkaline CO electro-oxidation on Cu and Au single crystals. Among the four Cu SCs explored, Cu(111) emerged as the best candidate having favorable thermodynamics i.e., an overpotential of only 150 mV (at 0.1 mA/cm²) compared to 370 mV

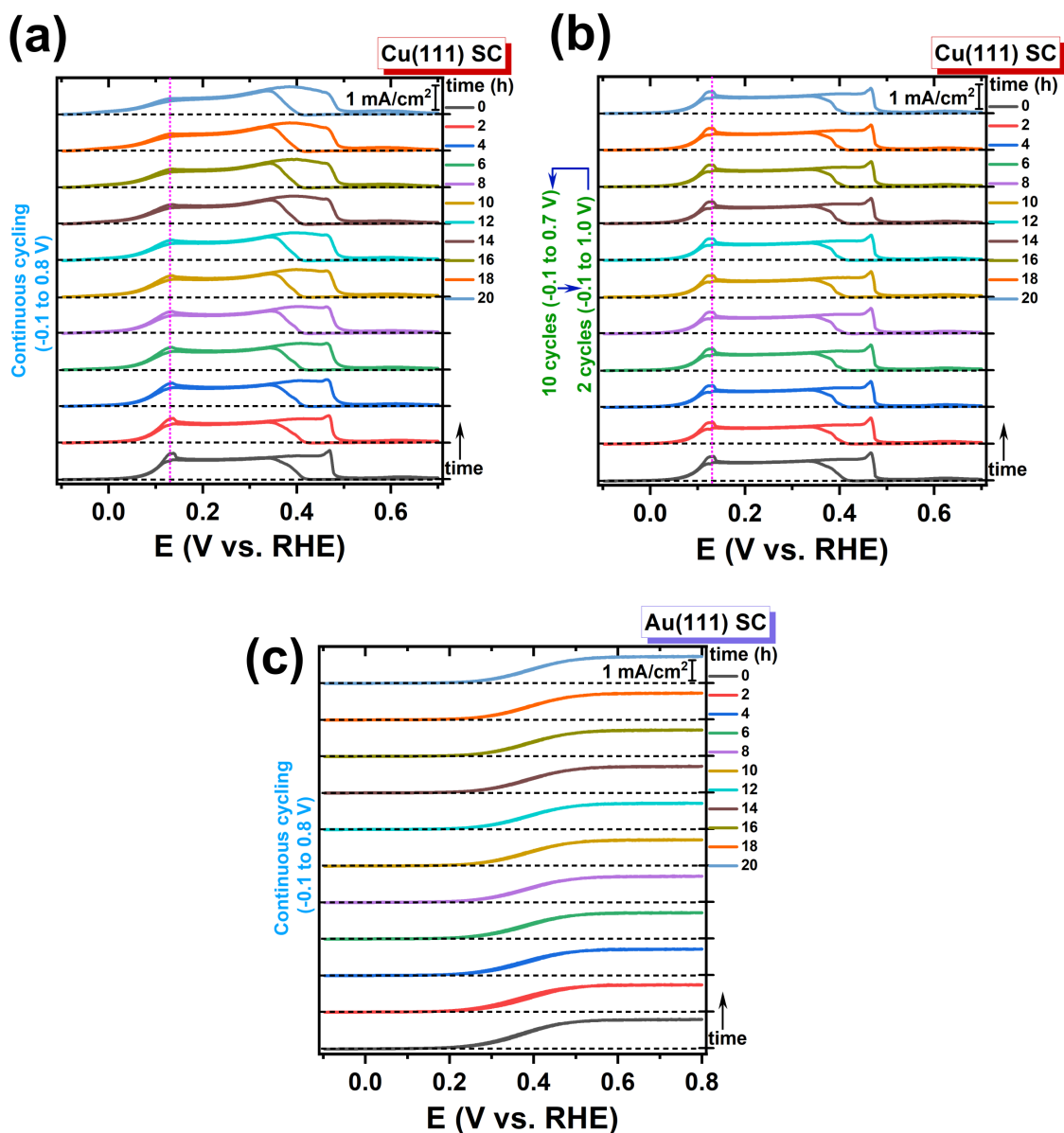


Figure 4: CO oxidation stability measurement under potentiodynamic conditions in the potential range of (a) -0.1 to +0.7 V for 20 h and (b) -0.1 to +0.7 V for 10 cycles followed by 2 cycles from -0.1 to +1.0 V for 2 cycles both repeated cyclically for 20 h on Cu(111); and (c) -0.1 to +1.0 V on Au(111) for 20 h in CO saturated (solid traces) and Ar saturated (dashed traces) 0.1 M KOH respectively at a scan rate of 25 mV/s.

for Au(111) and 410 mV for Au(100), and an optimal kinetics i.e., a high e-COOR current density of 0.97 mA/cm^2 (at 900 rpm) that is well within an order of magnitude compared to Au SCs. On the basis of Koutecky-Levich analysis and DFT based microkinetic modeling, we find e-COOR on Cu(111) to follow a Langmuir–Hinshelwood type chemical $^*\text{CO}-^*\text{OH}$ coupling, while on Au(111), it proceeds via an electrochemical Eley–Rideal type $^*\text{CO}-\text{OH}^-$ coupling. In particular, moderate binding energy of CO, co-existence of $^*\text{OH}$ and $^*\text{CO}$ on Cu(111) at relevant potentials, and their facile coupling barrier results in the high activity of Cu surfaces towards alkaline e-COOR. A combined reset-reaction profile allowed us to obtain a highly reproducible and retained CO electro-oxidation activity on Cu(111) for 20 h, comparable to Au(111). The details of the presented work, provide an in-depth comparison of the activity and stability of earth abundant Cu to the well-known Au electrocatalyst for alkaline e-COOR. These insights have potential applicability towards electrosynthesis of industrially important organic molecules and fuel cell applications.

Code & Data availability

The CatMAP input files, the DFT optimized structures and NEB trajectories, and the transport model used for the microkinetic simulations will be made available on the [CatTheory](#) Github account upon publication.

Acknowledgements

The computational work was supported by a research grant (29450) from VILLUM FONDEN. The experimental work by European Union’s Horizon 2020 research and innovation programme under the Marie Skłodowska-Curie grant agreement no. 713683.

Supporting Information Available

Additional details on the experiments, DFT simulations and microkinetic model.

References

- (1) Freund, H. J.; Meijer, G.; Scheffler, M.; Schlögl, R.; Wolf, M. CO oxidation as a prototypical reaction for heterogeneous processes. *Angewandte Chemie - International Edition* **2011**, *50*, 10064–10094.
- (2) Rodriguez, P.; Kwon, Y.; Koper, M. T. The promoting effect of adsorbed carbon monoxide on the oxidation of alcohols on a gold catalyst. *Nature Chemistry* **2012**, *4*, 177–182.
- (3) Chen, D. J.; Tong, Y. Y. *Encyclopedia of Interfacial Chemistry: Surface Science and Electrochemistry*; Elsevier, 2018; pp 881–897.
- (4) Rodriguez, P.; Koper, M. T. M. Electrocatalysis on gold. *Phys. Chem. Chem. Phys.* **2014**, *16*, 13583–13594.
- (5) Román, A. M.; Hasse, J. C.; Medlin, J. W.; Holewinski, A. Elucidating Acidic Electro-Oxidation Pathways of Furfural on Platinum. *ACS Catalysis* **2019**, *9*, 10305–10316.
- (6) Parsons, R.; VanderNoot, T. The oxidation of small organic molecules. A survey of recent fuel cell related research. *Journal of Electroanalytical Chemistry* **1988**, *257*, 9–45.
- (7) Rizo, R.; Arán-Ais, R. M.; Herrero, E. On the oxidation mechanism of C1-C2 organic molecules on platinum. A comparative analysis. *Current Opinion in Electrochemistry* **2021**, *25*, 100648.
- (8) Savinova, E.; Bonnefont, A.; Maillard, F. In *Encyclopedia of Applied Electrochemistry*; Kreysa, G., Ota, K.-i., Savinell, R. F., Eds.; Springer New York: New York, NY, 2014; pp 93–100.

- (9) Chen, D. J.; Tong, Y. Y. J. An in-situ electrochemical IR investigation of solution CO electro-oxidation on a polycrystalline Au surface in an alkaline electrolyte: Identification of active reaction intermediates. *Journal of Electroanalytical Chemistry* **2017**, *800*, 39–45.
- (10) Petrii, O. A. The Progress in Understanding the Mechanisms of Methanol and Formic Acid Electrooxidation on Platinum Group Metals (a Review). *Russian Journal of Electrochemistry* **2019**, *55*, 1–33.
- (11) Valdés-López, V. F.; Mason, T.; Shearing, P. R.; Brett, D. J. Carbon monoxide poisoning and mitigation strategies for polymer electrolyte membrane fuel cells – A review. *Progress in Energy and Combustion Science* **2020**, *79*, 100842.
- (12) Liu, Z.; Ma, L.; Zhang, J.; Hongsirikarn, K.; Goodwin, J. G. Pt alloy electrocatalysts for proton exchange membrane fuel cells: A review. *Catalysis Reviews - Science and Engineering* **2013**, *55*, 255–288.
- (13) Liu, Z.; Huang, Z.; Cheng, F.; Guo, Z.; Wang, G.; Chen, X.; Wang, Z. Efficient dual-site carbon monoxide electro-catalysts via interfacial nano-engineering. *Scientific Reports* **2016**, *6*, 33127.
- (14) Watanabe, M.; Motoo, S. Electrocatalysis by ad-atoms: Part III. Enhancement of the oxidation of carbon monoxide on platinum by ruthenium ad-atoms. *Journal of Electroanalytical Chemistry and Interfacial Electrochemistry* **1975**, *60*, 275–283.
- (15) Lin, W.; Iwasita, T.; Vielstich, W. Catalysis of CO Electrooxidation at Pt, Ru, and PtRu Alloy. An in Situ FTIR Study. *The Journal of Physical Chemistry B* **1999**, *103*, 3250–3257.
- (16) Watanabe, M.; Motoo, S. Electrocatalysis by ad-atoms: Part II. Enhancement of the oxidation of methanol on platinum by ruthenium ad-atoms. *Journal of Electroanalytical Chemistry and Interfacial Electrochemistry* **1975**, *60*, 267–273.

- (17) Marković, N. M.; Gasteiger, H. A.; Ross, P. N.; Jiang, X.; Villegas, I.; Weaver, M. J. Electro-oxidation mechanisms of methanol and formic acid on Pt-Ru alloy surfaces. *Electrochimica Acta* **1995**, *40*, 91–98.
- (18) Rodriguez, P.; Garcia-Araez, N.; Koverga, A.; Frank, S.; Koper, M. T. CO electrooxidation on gold in alkaline media: A combined electrochemical, spectroscopic, and DFT study. *Langmuir* **2010**, *26*, 12425–12432.
- (19) Kita, H.; Nakajima, H.; Hayashi, K. Electrochemical oxidation of CO on Au in alkaline solution. *Journal of Electroanalytical Chemistry* **1985**, *190*, 141–156.
- (20) Edens, G. J.; Hamelin, A.; Weaver, M. J. Mechanism of Carbon Monoxide Electrooxidation on Monocrystalline Gold Surfaces: Identification of a Hydroxycarbonyl Intermediate. *The Journal of Physical Chemistry* **1996**, *100*, 2322–2329.
- (21) Tiwari, A.; Heenen, H. H.; Bjørnlund, A. S.; Hochfilzer, D.; Chan, K.; Horch, S. Electrochemical Oxidation of CO on Cu Single Crystals under Alkaline Conditions. *ACS Energy Letters* **2020**, *5*, 3437–3442.
- (22) Auer, A.; Andersen, M.; Wernig, E. M.; Hörmann, N. G.; Buller, N.; Reuter, K.; Kunze-Liebhäuser, J. Self-activation of copper electrodes during CO electro-oxidation in alkaline electrolyte. *Nature Catalysis* **2020**, *3*, 797–803.
- (23) Tiwari, A.; Heenen, H. H.; Bjørnlund, A. S.; Maagaard, T.; Cho, E.; Chorkendorff, I.; Kristoffersen, H. H.; Chan, K.; Horch, S. Fingerprint Voltammograms of Copper Single Crystals under Alkaline Conditions: A Fundamental Mechanistic Analysis. *The Journal of Physical Chemistry Letters* **2020**, *11*, 1450–1455.
- (24) Tiwari, A.; Maagaard, T.; Chorkendorff, I.; Horch, S. Effect of Dissolved Glassware on the Structure-Sensitive Part of the Cu(111) Voltammogram in KOH. *ACS Energy Letters* **2019**, *4*, 1645–1649.

- (25) Wiberg, G. K. H.; Arenz, M. Establishing the potential dependent equilibrium oxide coverage on platinum in alkaline solution and its influence on the oxygen reduction. *Journal of Power Sources* **2012**, *217*, 262–267.
- (26) Gauthier, J. A.; Ringe, S.; Dickens, C. F.; Garza, A. J.; Bell, A. T.; Head-Gordon, M.; Nørskov, J. K.; Chan, K. Challenges in Modeling Electrochemical Reaction Energetics with Polarizable Continuum Models. *ACS Catalysis* **2019**, *9*, 920–931.
- (27) Stegelmann, C.; Andreasen, A.; Campbell, C. T. Degree of Rate Control: How Much the Energies of Intermediates and Transition States Control Rates. *Journal of the American Chemical Society* **2009**, *131*, 8077–8082, PMID: 19341242.
- (28) Maagaard, T.; Tiwari, A.; Chorkendorff, I.; Horch, S. On the Possibilities and Considerations of Interfacing Ultra-High Vacuum Equipment with an Electrochemical Setup. *ChemPhysChem* **2019**, *20*, 3024–3029.
- (29) Kunze-Liebhäuser, J. *Encyclopedia of Interfacial Chemistry*; Elsevier, 2018; pp 107–120.
- (30) Kunze, J.; Maurice, V.; Klein, L. H.; Strehblow, H. H.; Marcus, P. In situ STM study of the duplex passive films formed on Cu(111) and Cu(001) in 0.1 M NaOH. *Corrosion Science* **2004**, *46*, 245–264.

Supporting Information:

Alkaline CO electro-oxidation: Mechanistic Differences between Copper and Gold Single Crystals and Peculiarities of various Copper Facets

Aarti Tiwari,^{†,‡,||} Nitish Govindarajan,^{¶,||} Hendrik H. Heenen,[¶] Anton Bjørnlund,[†]
Karen Chan,^{*,¶} and Sebastian Horch^{*,†,§}

[†]*SurfCat, Department of Physics, Technical University of Denmark, 2800 Kgs. Lyngby, Denmark*

[‡]*Interface Science Department, Fritz-Haber Institute of the Max Planck Society, 14195 Berlin, Germany*

[¶]*Catalysis Theory Center, Department of Physics, Technical University of Denmark, 2800 Kgs. Lyngby, Denmark*

[§]*Department of Engineering Technology, Technical University of Denmark, 2750 Ballerup, Denmark*

|| These authors contributed equally to this work

E-mail: kchan@fysik.dtu.dk; shor@dtu.dk

1 Experimental CVs and polarization curves

1.1 Experimental Methods

The electrochemical cell used for the measurements is a one compartment, 3-electrode PTFE cell (Pine Research, detailed elsewhere^{? ?}) wrapped in an Ar-filled air bag. The Cu and Au SC working electrodes [Mateck, Jülich (DE); purity 99.9999%; typical diameter of exposed surface is 6 mm; thickness 3 mm] were housed in a custom built PTFE-holder compatible with the Pine Research rotator's RDE shaft.[?] The counter electrode employed was a Ni mesh (10.5 cm²) and all the potentials were referenced against a reversible hydrogen electrode (RHE). All the electrochemical measurements were performed by a Bio-Logic SP200 potentiostat run by Bio-Logic's EC-Lab software. Prior to measurements, the Cu SCs were electropolished for 60 s in a 66% H₃PO₄ solution (85% EMSURE, Merck) at 2.0 V (vs. Cu wire; Goodfellow, purity 99.9%) whereas Au SCs were first flame annealed and then electropolished for 60 s at 2.4 V (vs. Au wire; Goodfellow, purity 99.99+%) followed by a thorough rinsing with Millipore water (18.2 MΩ · cm). The electrolyte was a 0.1 M KOH solution (99.995 Suprapur, Merck) prepared in a PFA volumetric flask (Corning Life Sciences) using Millipore water. The gases used for purging were Ar (6.0, Air Liquide) for blank measurements as well as in the air bag, and CO (5.0, Air Liquide) passed through a carbonyl trap (Leiden Probe Microscopy) for the CO oxidation measurements. It should be noted here that high purity gases were found essential to obtain the long-term CO oxidation response observed. The cleanliness state of the measurements was continuously monitored by performing ICP analysis of the electrolyte and *ex situ* XPS analysis of the SCs to rule out any trace contamination, especially due to the presence of metallic impurities. The reproducibility of the measurements was ascertained by repeating them at least three times. All the presented data in the article are as obtained and without any baseline correction.

The upper limit in potential for the Cu CVs were chosen to incorporate OH adsorption features but to avoid surface oxidation, while the lower limit on potential was chosen to

avoid hydrogen evolution reaction (HER). These bounds define the fingerprint region that identifies the surface orientation of Cu.⁷ The CVs for Au were also measured in a similar range for better comparison with Cu. However, a full range CV (from 0 V to 1.5 V vs. RHE) for Au is shown in Figure S2 (SI) to compare with previous reports.

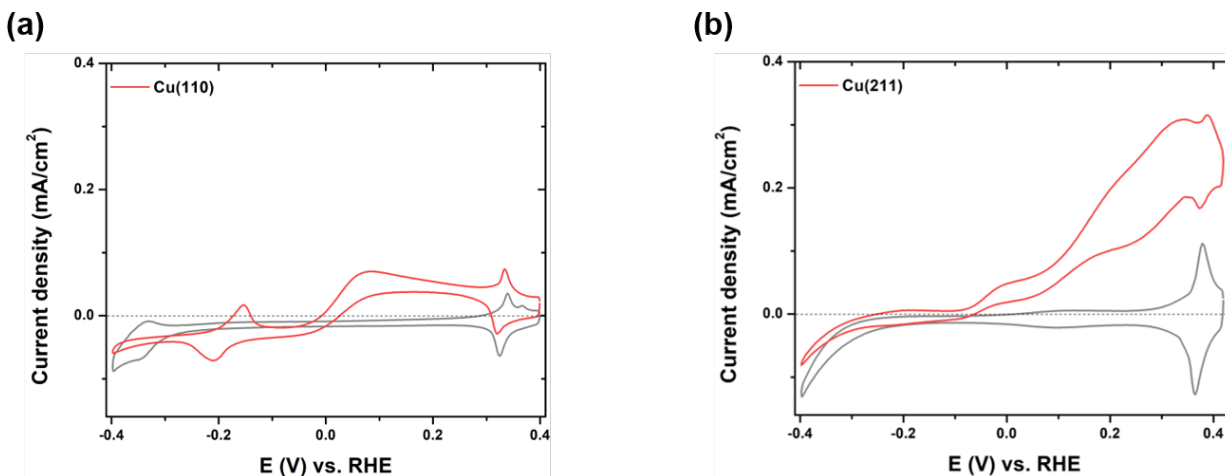


Figure S1: Cyclic voltammograms for (a) Cu(110), and (b) Cu(211) single crystals in their respective fingerprint regions measured in blank Ar-saturated (grey trace) and CO-saturated (red trace) 0.1 M KOH at a scan rate of 50 mV/s.

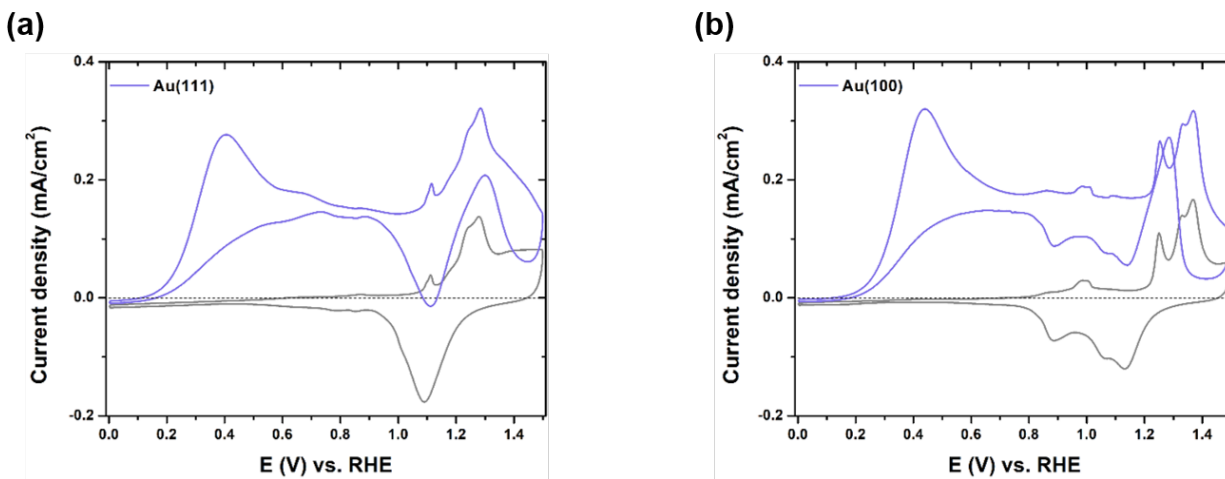


Figure S2: Cyclic voltammograms for (a) Au(111), and (b) Au(100) single crystals measured in blank Ar-saturated (grey trace) and CO-saturated (red trace) 0.1 M KOH at a scan rate of 50 mV/s.

Table S1: Experimentally observed onset (E_{onset}) and overpotentials (η) corresponding to $25 \mu\text{A}/\text{cm}^2$ obtained from the cyclic voltammograms in Figure 1 b & c (Main text) and Figure S1 & S2 (SI). The choice of current density i.e. $25 \mu\text{A}/\text{cm}^2$ instead of $1 \text{ mA}/\text{cm}^2$ used in the main text is due to the low obtainable currents on the Cu(110) surface.

<i>Surface</i>	$E_{\text{onset}}(\text{V})$	$\eta(\text{V})$
Au(111)	0.25	0.35
Au(100)	0.28	0.38
Cu(111)	0.04	0.14
Cu(100)	-0.07	0.03
Cu(110)	0.02	0.12
Cu(211)	-0.05	0.05

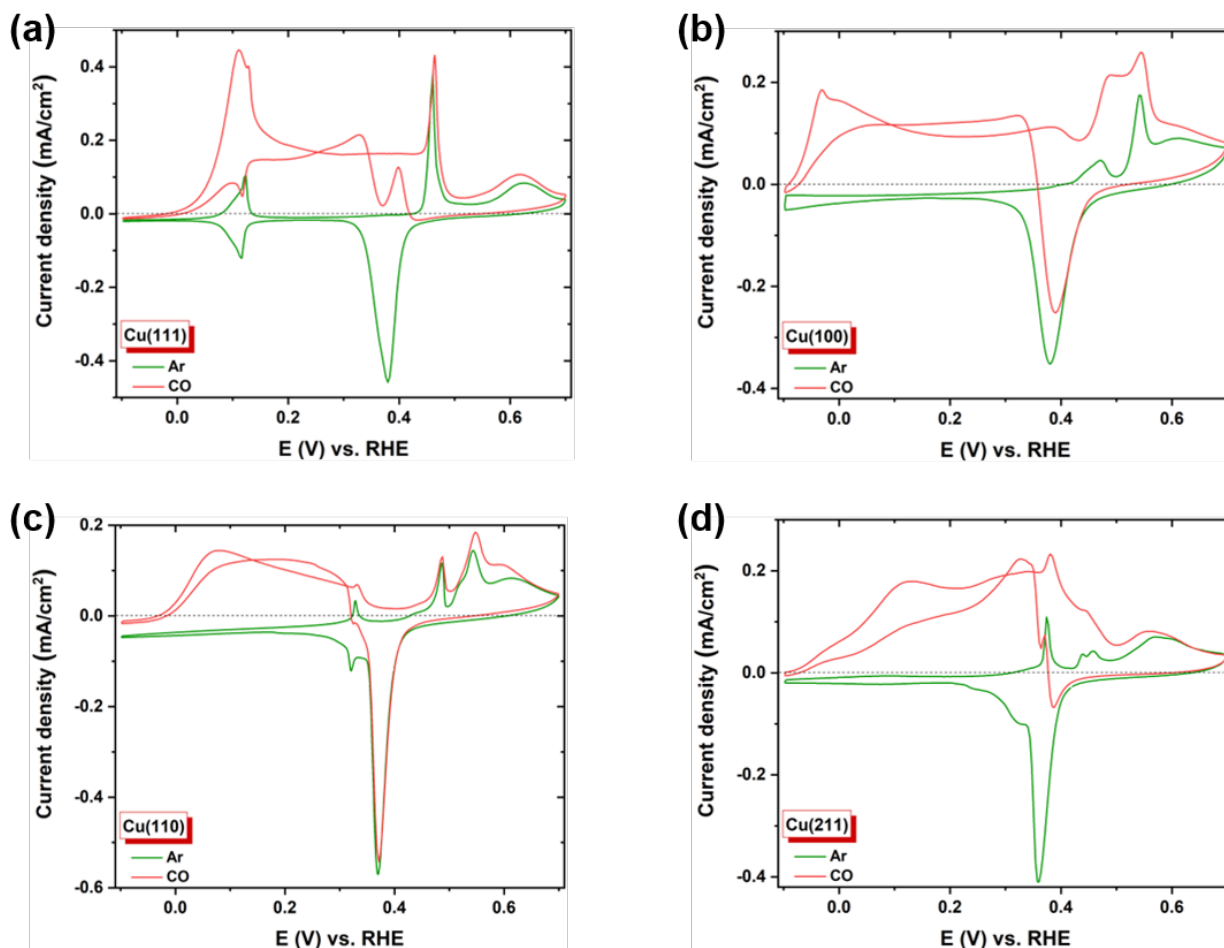


Figure S3: Polarization curves at 0 rpm for (a) Cu(111), (b) Cu(100), (c) Cu(110), and (d) Cu(211) single crystals in Ar (green trace) and CO (red trace) saturated 0.1 M KOH at a scan rate of 25 mV/s. The observed increase in oxidation currents under static conditions (i.e. 0 rpm) in the presence of CO vs. Ar suggests the respective abilities of the different Cu facets towards e-COOR.

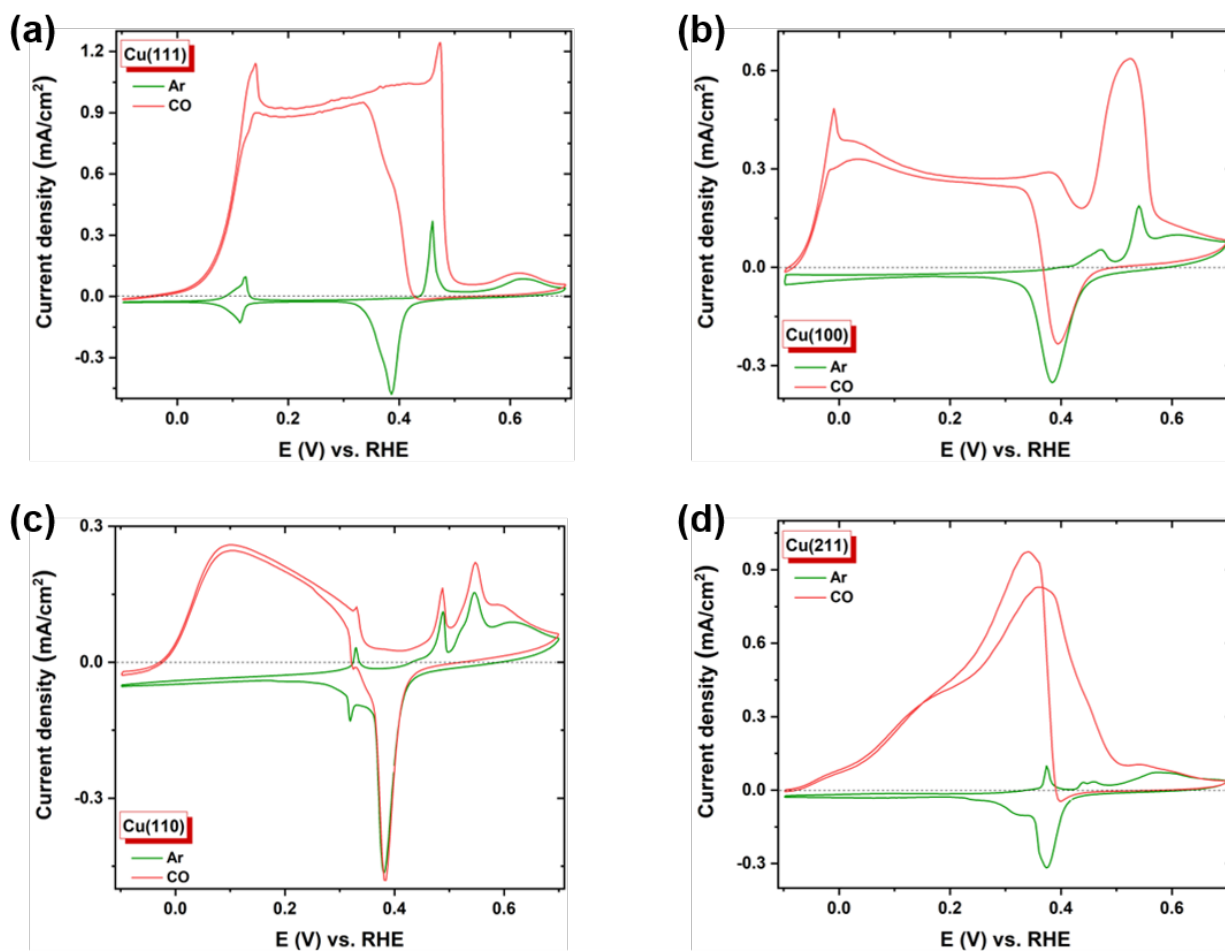


Figure S4: Polarization curves at 900 rpm for (a) Cu(111), (b) Cu(100), (c) Cu(110), and (d) Cu(211) single crystals in Ar (green trace) and CO (red trace) saturated 0.1 M KOH at a scan rate of 25 mV/s. A significant increase in oxidation current density compared to [Figure S3](#) depicts the influence of mass transport i.e. at 900 rpm (vs. 0 rpm) towards the respective Cu SCs e-COOR activity.

1.2 Details of RDE Features

Following the discussion of Cu(111) RDE response (main text), Cu(100) also shows an initial increase in CO oxidation current at ca. 0 V (Figure S4b), which is consistent with the observation from CV measurements (Figure 1c, main text). It is followed by the limiting current behavior before merging with the surface oxidation response at ca. 0.38 and 0.52 V, after which the CO oxidation current dies off as the surface is oxidized. The renewal in activity post surface reduction and a slight hysteresis is a similar observation to Cu(111) but with lower e-COOR current densities. Cu(110) SC also shows a similar trend but there is only a marginal influence of enhanced mass transport on the obtained current density (Figure 2c, main text). This observation suggests the significant influence of a lower *OH coverage and more importantly of the surface structure that results in the presence of *OH and *CO in close proximity enabling CO electro-oxidation.^{S1} Cu(211) also exhibits a similar response, but the only difference and an interesting observation is that the freshly reduced surface is highly active for CO oxidation. This characteristic is suggested by the higher obtainable oxidative current densities post surface reduction at ca. 0.34 V clearly seen upon enhanced mass transport of CO i.e., on increasing the rotation rate (rpm). In addition, the fact that CO is essential for the observed oxidative response is reflected clearly from Figure S6 depicting no difference between the RDE trace at both 0 and 900 rpm in blank Ar-saturated electrolyte for all the four Cu facets.

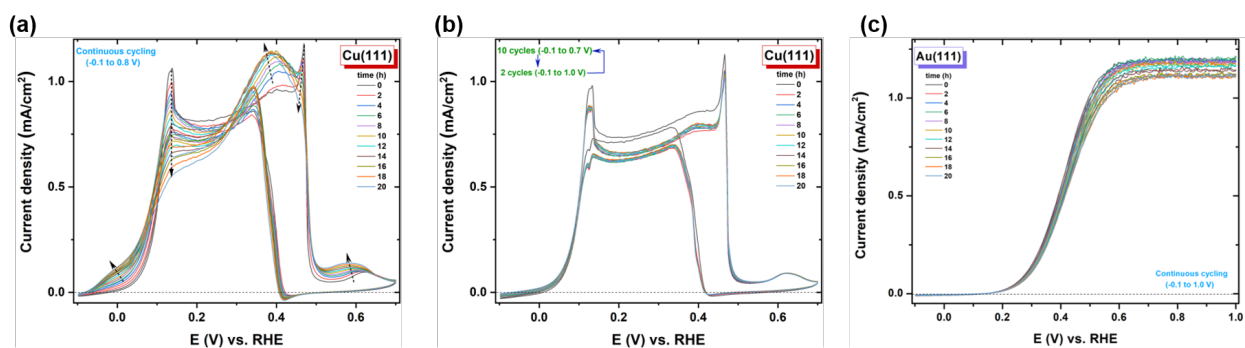


Figure S5: CO oxidation stability measurement under potentiodynamic conditions in the potential range of (a) -0.1 to +0.7 V for 20 h and (b) -0.1 to +0.7 V for 10 cycles (reaction profile) followed by from -0.1 to +1.0 V for 2 cycles (reset profile) both profiles repeated cyclically for 20 h on Cu(111); and (c) -0.1 to +1.0 V on Au(111) for 20 h in CO saturated 0.1 M KOH at a scan rate of 25 mV/s. The possibility of e-COOR activity retention for Cu(111) is depicted following a reset-reaction potential profile compared to a simple long term activity measurement. Similar measurements for Au(111) shows no need of such potential profiles and its retained long term activity.

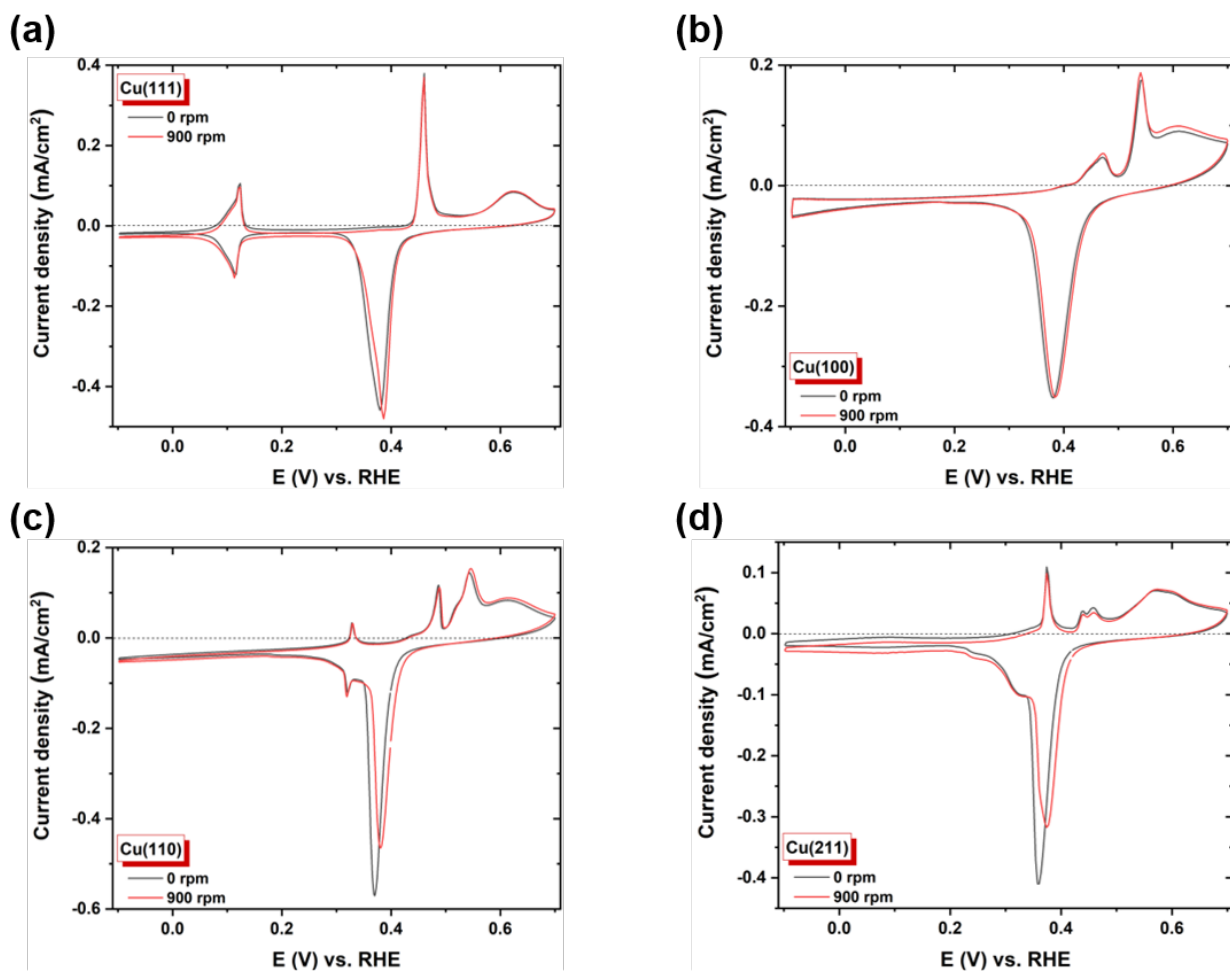


Figure S6: Polarization curves compared at 0 & 900 rpm for (a) Cu(111), (b) Cu(100), (c) Cu(110), and (d) Cu(211) single crystals in Ar saturated 0.1 M KOH at a scan rate of 25 mV/s. These show that the oxidation currents observed in Figure 2 a & b (main text), Figure 3 (main text), [Figure S3](#) (SI) and [Figure S4](#) (SI) are only due to CO oxidation without any artefact from the RDE measurements itself.

2 Computational Methods

DFT calculations were performed using Quantum Espresso^{S2} with the BEEF-vdW exchange-correlation functional.^{S3} The plane-wave and density cutoffs used were 500 and 5000 eV respectively. A Fermi-smearing width of 0.1 eV was used, and the electronic structure was converged until the total energy difference was $< 10^{-5}$ eV. Solvation effects were included via the self-consistent continuum solvation (SCCS) model as implemented in the Environ package.^{S4} We used the standard “fitg03” parameters ($\rho_{(\min)}=0.0001$, $\rho_{(\max)}=0.005$, $\alpha + \gamma=11.5$ dyn/cm). Symmetric 3x4 slabs were used to simulate adsorbates on Cu(111) and Au(111) surfaces with a vacuum spacing of 12 Å. The Brillouin zone was sampled via a $4 \times 3 \times 1$ Monkhorst-Pack grid.^{S5} Nonsymmetric slab models were used for nudged-elastic-band (NEB) calculations.^{S6,S7} The most stable adsorption sites for all adsorbates were identified through sampling of all symmetrically inequivalent adsorption sites as identified using the CatKit package.^{S8} Barrier calculations were performed using the NEB method and handled by AID-NEB.^{S9,S10} The barriers were computed with a minimal accuracy of the surrogate model of 25 meV and convergence of the forces on the climbing image of 25-50 meV. All transition states were confirmed to have a single imaginary frequency. Free energies were obtained following the ideal gas law for gas phase molecules and the harmonic oscillator model for the adsorbates, respectively. All energies were referenced to gas-phase H₂ (1 atm), CO (1 atm) and H₂O at the vapor pressure of liquid water (0.035 atm). To mitigate systematic DFT errors, we used corrections of 0.15 eV per C=O double bond and 0.1 eV for the H₂(g) reference as suggested by Christensen et al.^{S11} Electrochemical reaction energetics were referenced using the Computational Hydrogen Electrode (CHE) formalism.[?]

3 Computed reaction barriers on Cu(111)

The energy profiles of the minimum energy pathway calculated using the NEB method for the *CO-*OH and *COOH-*OH coupling reactions on Cu(111) are provided in [Figure S7](#).

Insets depict atomic configurations of key images along the NEB.

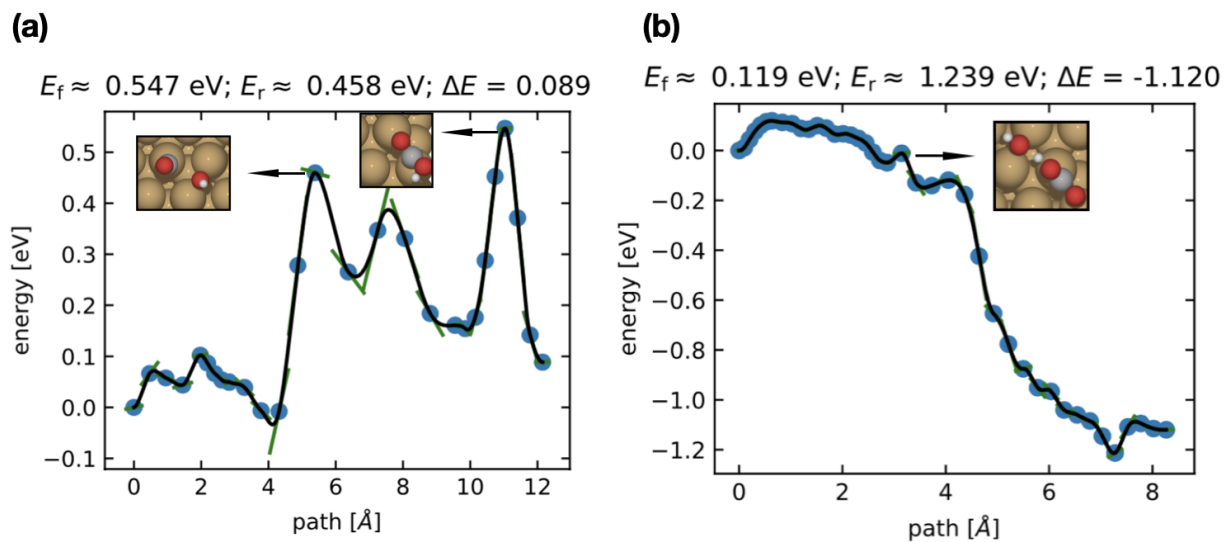


Figure S7: Potential energy profile from the converged NEB simulations for (a) the *CO-*OH coupling and (b) *COOH-*OH coupling on Cu(111). The blue points correspond to the energy of an individual NEB image and the green lines represent the forces (gradients). Transition states correspond to the image with the highest energy in the profile. Insets depict the atomic configuration of selected images along the pathway. E_f , E_r , and ΔE correspond to the forward barrier, reverse barrier and the energetic difference between the product and reactant states.

4 Free energy profiles for e-COOR on Cu(111) and Au(111)

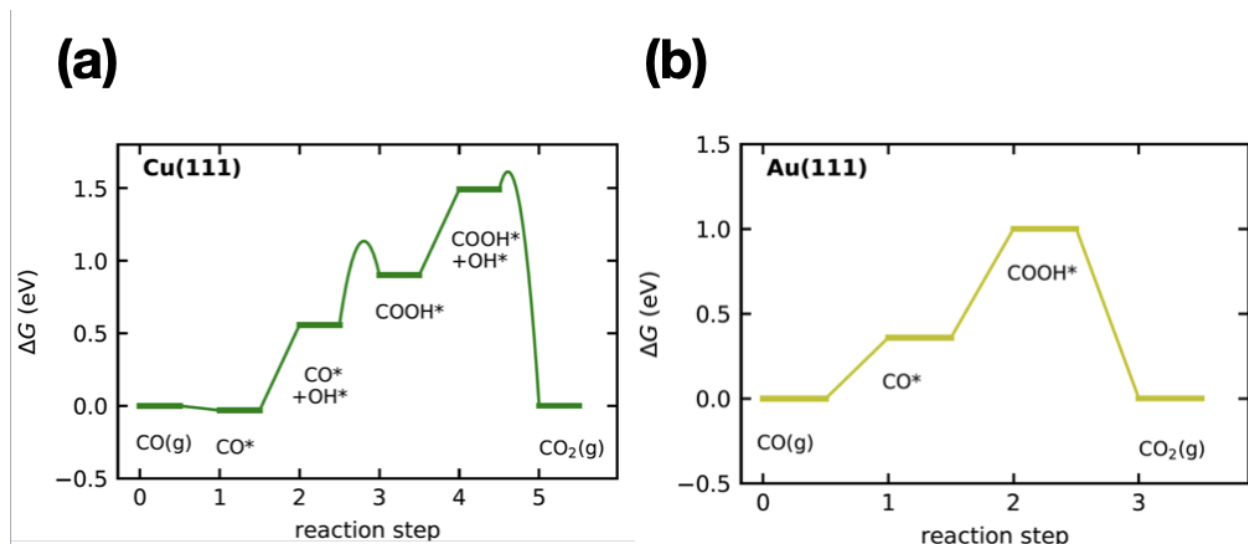


Figure S8: Free energy diagrams for the e-COOR on (a) Cu(111) and (b) Au(111) at the thermodynamic equilibrium potential ($U = -0.22$ V vs RHE) as predicted by DFT.

5 Approximation of the CO-OH^- electrochemical barrier

Decisive to the simulated polarization curves obtained using the microkinetic model are the barriers for the rate-determining step (RDS) in the reaction. For the example of CO oxidation on Au(111), where the RDS is clearly defined as the CO-OH^- coupling step (see Figure S8), the barrier corresponds to an electrochemical reaction which cannot be reliably assessed.^{S12} To this end, we estimate it using the data obtained from the RDE experiments on Au(111). In particular, we fit the simulated current density from the microkinetic model to match the kinetic current density and Tafel slope obtained for Au(111) using the Levich analysis in Figure 2d (main text). The fitted barrier obtained for the electrochemical coupling of CO-OH^- is ca. 0.6 eV. In addition, the charge transfer co-efficient, β for this coupling step was assumed to be 0.5.

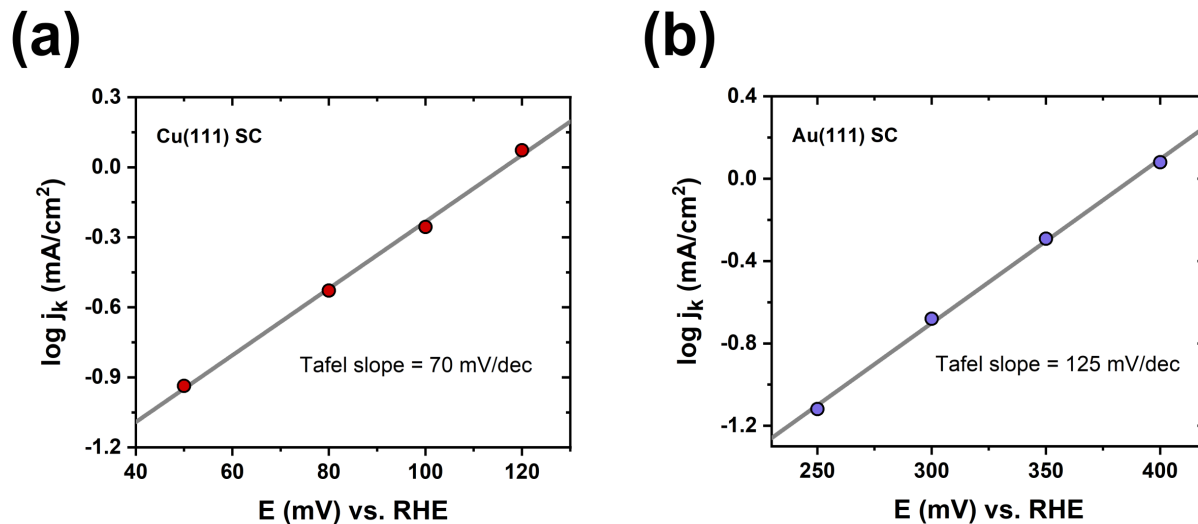


Figure S9: Tafel plot for (a) Cu(111) and (b) Au(111) using the Levich analysis in Figure 2c & 2d (main text) respectively.

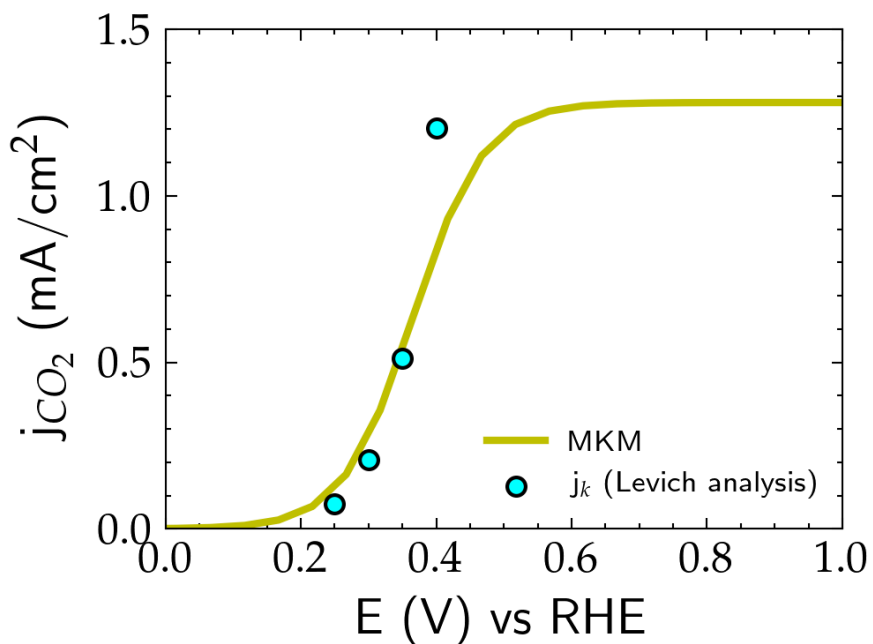


Figure S10: Simulated current density for e-COOR on Au(111) obtained using the microkinetic model (MKM) with an adjusted barrier for CO-OH^- obtained by fitting to the kinetic current density (j_k) obtained using the Levich analysis on Au(111).

6 Details of the microkinetic model

Microkinetic simulations were performed using the CatMAP package^{S13} by using the DFT energetics as input. CatMAP solves the kinetic rate equations using the steady-state approximation in order to estimate species consumption, adsorbate coverages and production rates. The reactions shown in Eqns. (2)-(5) and (6)-(8) in the main text were used in the microkinetic model for e-COOR on Cu(111) and Au(111), respectively. A pre-exponential factor of 10^{13} s^{-1} as obtained from transition-state theory^{S14} was used for all the reaction steps. Current density towards CO_2 production (j_{CO_2}) was obtained from TOF_{CO_2} using Equation (1) following Ref.^{S15}

$$j_{\text{CO}_2} = 2e\rho\text{TOF}_{\text{CO}_2} \tag{1}$$

$$e\rho = 80.3\mu\text{C}/\text{cm}^2 \tag{2}$$

In order to account for the mass transport of the reactant CO species, we used Fick’s first law to estimate its flux (J_{CO}) at the interface (cf. Equation (3)). The diffusion coefficient of CO was taken to be $20.3 \times 10^{-10} \text{ m}^2/\text{s}$.^{S16} The concentration of dissolved CO ($\text{CO}(\text{aq})$) is estimated from the Henry constant ($1100 \text{ L}\cdot\text{atm}\cdot\text{mol}^{-1}$)^{S17} and Henry’s law is used to estimate the corresponding pressure of $\text{CO}(\text{g})$.

$$J_{\text{CO}} = -D_{\text{CO}} \frac{dc}{dx} \tag{3}$$

A self-consistent cycle is run between CatMAP and the analytical diffusion model. The species consumption and product rates are estimated using the microkinetic rate equations solved by CatMAP. The product rates obtained from the CatMAP model correspond to the turn-over-frequency (TOF) of an individual catalytic site. The TOF is then converted to

molar fluxes using a site-density corresponding to the unit cell of the Cu(111) and Au(111) facets. These fluxes then serve as an input for the analytical model given by Equation (3) to obtain the CO concentration at the interface that is in turn used as the input in the CatMAP model. The microkinetic and transport models are then solved iteratively until a tolerance of 10^{-2} is achieved.

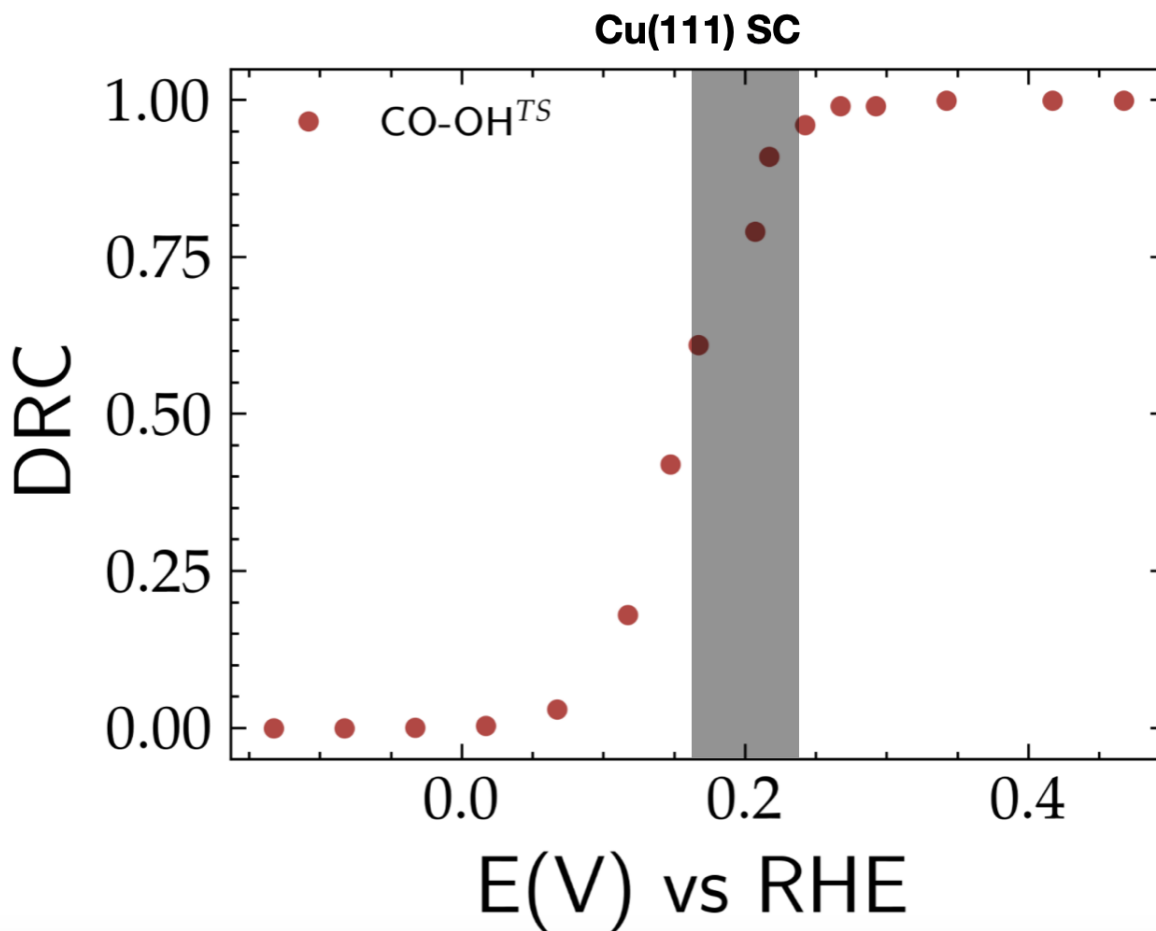


Figure S11: Simulated degree of rate control (DRC) obtained from the microkinetic simulations for the $^*\text{CO}-^*\text{OH}^{TS}$ transition state (TS) on the overall CO_2 production rate on the Cu(111) surface denoted as Cu(111) SC. A positive DRC value indicates that the intermediate has to be stabilized in order to increase the rate, and a DRC value of 1 corresponding to full rate control of the intermediate. The shaded region represents potentials close to the onset of e-COOR where the $^*\text{CO}-^*\text{OH}^{TS}$ dominates the overall rate of e-COOR.

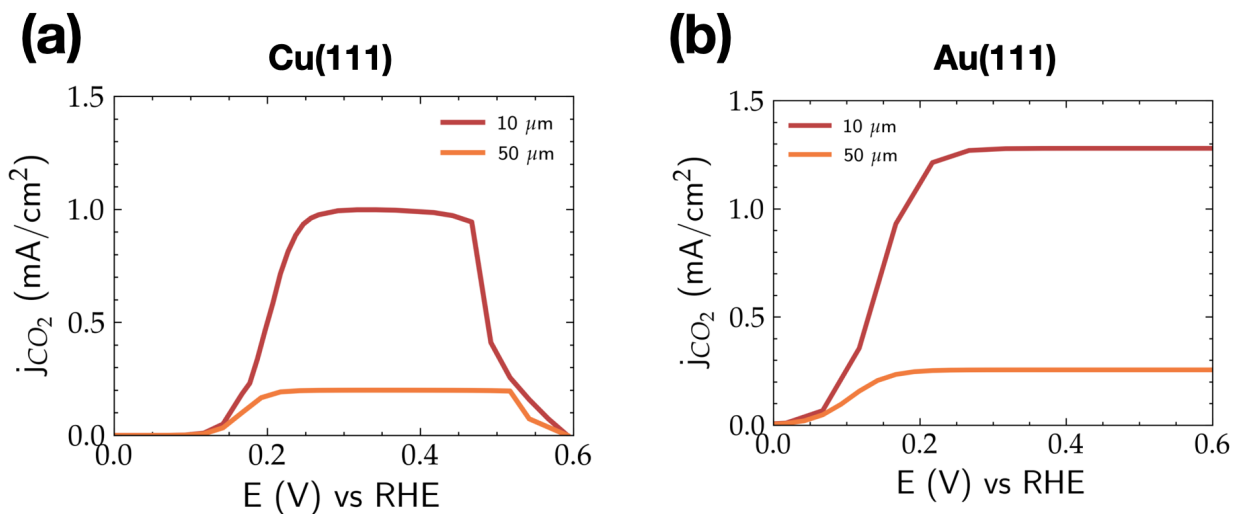


Figure S12: Sensitivity of the simulated CO₂ polarization curves to the boundary layer thickness for (a) Cu(111) and (b) Au(111) single crystals.

References

- (S1) Tiwari, A.; Heenen, H. H.; Bjørnlund, A. S.; Hochfilzer, D.; Chan, K.; Horch, S. Electrochemical Oxidation of CO on Cu Single Crystals under Alkaline Conditions. *ACS Energy Letters* **2020**, *5*, 3437–3442.
- (S2) Giannozzi, P.; Baroni, S.; Bonini, N.; Calandra, M.; Car, R.; Cavazzoni, C.; Ceresoli, D.; Chiarotti, G. L.; Cococcioni, M.; Dabo, I.; Corso, A. D.; de Gironcoli, S.; Fabris, S.; Fratesi, G.; Gebauer, R.; Gerstmann, U.; Gougoussis, C.; Kokalj, A.; Lazzeri, M.; Martin-Samos, L.; Marzari, N.; Mauri, F.; Mazzarello, R.; Paolini, S.; Pasquarello, A.; Paulatto, L.; Sbraccia, C.; Scandolo, S.; Sclauzero, G.; Seitsonen, A. P.; Smogunov, A.; Umari, P.; Wentzcovitch, R. M. QUANTUM ESPRESSO: a modular and open-source software project for quantum simulations of materials. *Journal of Physics: Condensed Matter* **2009**, *21*, 395502.
- (S3) Wellendorff, J.; Lundgaard, K. T.; Møgelhøj, A.; Petzold, V.; Landis, D. D.; Nørskov, J. K.; Bligaard, T.; Jacobsen, K. W. Density functionals for surface sci-

- ence: Exchange-correlation model development with Bayesian error estimation. *Phys. Rev. B* **2012**, *85*, 235149.
- (S4) Andreussi, O.; Dabo, I.; Marzari, N. Revised self-consistent continuum solvation in electronic-structure calculations. *The Journal of Chemical Physics* **2012**, *136*, 064102.
- (S5) Monkhorst, H. J.; Pack, J. D. Special points for Brillouin-zone integrations. *Phys. Rev. B* **1976**, *13*, 5188–5192.
- (S6) Henkelman, G.; Uberuaga, B. P.; Jónsson, H. A climbing image nudged elastic band method for finding saddle points and minimum energy paths. *The Journal of Chemical Physics* **2000**, *113*, 9901–9904.
- (S7) Henkelman, G.; Jónsson, H. Improved tangent estimate in the nudged elastic band method for finding minimum energy paths and saddle points. *The Journal of Chemical Physics* **2000**, *113*, 9978–9985.
- (S8) Boes, J. R.; Mamun, O.; Winther, K.; Bligaard, T. Graph Theory Approach to High-Throughput Surface Adsorption Structure Generation. *The Journal of Physical Chemistry A* **2019**, *123*, 2281–2285, PMID: 30802053.
- (S9) Larsen, A. H.; Mortensen, J. J.; Blomqvist, J.; Castelli, I. E.; Christensen, R.; Dułak, M.; Friis, J.; Groves, M. N.; Hammer, B.; Hargus, C.; Hermes, E. D.; Jennings, P. C.; Jensen, P. B.; Kermode, J.; Kitchin, J. R.; Kolsbjerg, E. L.; Kubal, J.; Kaasbjerg, K.; Lysgaard, S.; Maronsson, J. B.; Maxson, T.; Olsen, T.; Pastewka, L.; Peterson, A.; Rostgaard, C.; Schiøtz, J.; Schütt, O.; Strange, M.; Thygesen, K. S.; Vegge, T.; Vilhelmsen, L.; Walter, M.; Zeng, Z.; Jacobsen, K. W. The atomic simulation environment—a Python library for working with atoms. *Journal of Physics: Condensed Matter* **2017**, *29*, 273002.
- (S10) Garrido Torres, J. A.; Jennings, P. C.; Hansen, M. H.; Boes, J. R.; Bligaard, T. Low-

- Scaling Algorithm for Nudged Elastic Band Calculations Using a Surrogate Machine Learning Model. *Phys. Rev. Lett.* **2019**, *122*, 156001.
- (S11) Christensen, R.; Hansen, H. A.; Vegge, T. Identifying systematic DFT errors in catalytic reactions. *Catal. Sci. Technol.* **2015**, *5*, 4946–4949.
- (S12) Gauthier, J. A.; Ringe, S.; Dickens, C. F.; Garza, A. J.; Bell, A. T.; Head-Gordon, M.; Nørskov, J. K.; Chan, K. Challenges in Modeling Electrochemical Reaction Energetics with Polarizable Continuum Models. *ACS Catalysis* **2019**, *9*, 920–931.
- (S13) Medford, A. J.; Shi, C.; Hoffmann, M. J.; Lausche, A. C.; Fitzgibbon, S. R.; Bliigaard, T.; Nørskov, J. K. CatMAP: A Software Package for Descriptor-Based Microkinetic Mapping of Catalytic Trends. *Catalysis Letters* **2015**, *145*, 794–807.
- (S14) *Fundamental Concepts in Heterogeneous Catalysis*; John Wiley & Sons, Ltd, 2014.
- (S15) Hansen, H. A.; Viswanathan, V.; Nørskov, J. K. Unifying Kinetic and Thermodynamic Analysis of 2 e⁻ and 4 e⁻ Reduction of Oxygen on Metal Surfaces. *The Journal of Physical Chemistry C* **2014**, *118*, 6706–6718.
- (S16) Cussler, E. L.; Cussler, E. L. *Diffusion: mass transfer in fluid systems*; Cambridge university press, 2009.
- (S17) Sander, R. Compilation of Henry’s law constants (version 4.0) for water as solvent. *Atmospheric Chemistry and Physics* **2015**, *15*, 4399–4981.